



Practice article

Hardware-in-the-loop testing of simple and intelligent MPPT control algorithm for an electric vehicle charging power by photovoltaic system



Mohamed Fawzy El-Khatib^{a,b,*}, Mohamed-Nabil Sabry^b, Mohamed I. Abu El-Sebah^c, Shady A. Maged^b

^a Mechatronics and Robotics Engineering Department, Faculty of Engineering, Egyptian Russian University (ERU), Cairo 11829, Egypt

^b Mechatronics Engineering Department, Faculty of Engineering, Ain Shams University, Cairo 11517, Egypt

^c Power Electronics and Energy Conversion Department, Electronics Research Institute, Cairo 11843, Egypt

ARTICLE INFO

Article history:

Received 27 June 2022

Received in revised form 18 January 2023

Accepted 18 January 2023

Available online 23 January 2023

Keywords:

Photovoltaic

Fuzzy logic controller

Artificial neural network

Simplified universal intelligent PID controller

Particle swarm optimization

Electric vehicle battery

ABSTRACT

In this paper, an electric vehicle (EV) charging station powered by a photovoltaic (PV) system has been created to charge EVs. Furthermore, the maximum available power from the PV system was extracted using a new algorithm called the simplified universal intelligent PID (SUIPID) controller, which has the advantages of simplicity in design and intelligence. The SUIPID controller was compared to the artificial neural networks (ANNs), the fuzzy logic controller (FLC) based on linear membership functions, and the FLC based on particle swarm optimization (PSO) to optimize its parameters under various conditions. The system simulation was first performed using MATLAB software, then an experimental set up was conducted to confirm the theoretical work. The proposed SUIPID responds 28.5%, 44.4%, and 61.5% faster than the PSO-FLC, ANN, and FLC, respectively, whereas the ITAE error was reduced by 27.3%, 52.9%, and 65.2%, respectively. Also, the charging procedure of the EV battery is precisely steady under different atmospheric conditions. The SUIPID controller has several advantages over other intelligent algorithms, most notably its ease of design and implementation.

© 2023 ISA. Published by Elsevier Ltd. All rights reserved.

1. Introduction

Electric vehicles (EVs) are gradually displacing conventional internal combustion engine (ICE) vehicles, with a growing interest in charging solar energy. Indeed, ICEs have many disadvantages that are avoided by electric vehicles. EVs emit little pollution, are more energy-efficient, produce less noise, and require less maintenance than ICEs [1,2]. However, the charging procedure for an EV battery continues to face numerous hurdles, including charging time, charging station infrastructure, and the influence of charging stations on the existing electrical power supply. Renewable energy sources (RESs) have seen significant growth during the last few years to produce electricity to overcome the increase in electricity demand and reduce environmental impacts [3,4]. Consequently, RESs (using solar, wind, and hydro, for example) are gradually replacing conventional energy sources such as fossil fuels, natural gas, and nuclear [5,6]. Due to the huge amount of solar irradiation that covers the earth's surface and recent

technological advances that have reduced its cost, RESs based on photovoltaic energy are frequently used. However, photovoltaic systems may be inefficient at converting energy because their nonlinear characteristic curves are strongly impacted by temperature and solar irradiation [7,8].

Referring to Thevenin's theorem, the solar panel's resistance should be equivalent to the resistance of the load under all operating conditions in order to transfer the maximum amount of power to the load by connecting the photovoltaic system to the load via a DC-DC converter. Maximum power point tracking (MPPT) control techniques make use of a converter in order to adjust the operating point of the solar system until the maximum power point (MPP) is reached. There is a unique point on the power-voltage (P-V) curve, called the MPP, at which the PV system produces its maximum output power. Consequently, the maximum power is supplied to the required load, and the maximum system efficiency is achieved [9,10]. When a PV module is exposed to constant irradiance levels and temperatures, the system can be tuned for maximum power using any simple MPP device. However, under varying irradiance and temperature levels, the PV system needs a fast MPPT control algorithm in order to match the sudden changes in atmospheric conditions [11,12].

* Corresponding author at: Mechatronics and Robotics Engineering Department, Faculty of Engineering, Egyptian Russian University (ERU), Cairo 11829, Egypt.

E-mail address: muhamed-fawzy@eru.edu.eg (M.F. El-Khatib).

Thus, PV systems need to use an MPPT control algorithm to keep track of the MPP.

One way which has been commonly implemented to track the MPP is through conventional techniques such as incremental conductance (IC), perturb and observe (P&O), open-circuit voltage (OSV), short-circuit current (SCC), and others, as they are simple to design [11–14]. The P&O and IC methods suffer from substantial oscillations when tracking the MPP [11,12]. A slight change in solar irradiance necessitates that the method recalculates the best value of the control signal for MPP operation. Less time is required for recalculation, but this results in significant power loss. While the OSV and SCC approaches depend on numerical concepts and necessitate regular measurements of open-circuit voltage and short-circuit current readings in order to generate the necessary MPP value, the system's operation is disconnected [13]. In fact, the PV system always operates under varying irradiance levels and temperatures, and hence applying the conventional techniques will cause the wrong tracking of the MPP, decreasing the system efficiency as these techniques implement a fixed step size to get the MPP.

To overcome these problems, artificial intelligent algorithms such as ANNs, FLC adaptive neuro-fuzzy, and others have been proposed [15–18]. In the literature, the ANNs technique has a wide range of engineering applications. Since ANNs and FLC methods are thought to be able to solve problems related to simple P&O and IC MPPT methods, they are frequently used for MPPT applications in the PV energy system. In most FLC MPPT systems, the inputs to the controller are the error signal and power derivative error of the PV module. Derivatives minimize the complexity of computational, but generating complicated fuzzy inference rules is laborious. The effectiveness of the fuzzy algorithm can be diminished if the membership function values are not accurately predicted for the system under consideration [15]. ANNs gained popularity due to their capacity to detect complex nonlinear relationships between dependent and independent variables without requiring accurate mathematical modeling. Applying ANNs for MPPT enhanced PV array output power and yielded superior results [16–18]. Also, several optimization techniques based on natural mimics have been proposed such as the ant colony optimization (ACO) [19], PSO [20–22], the grey wolf optimization (GWO) [23,24], and others. The main objective of these algorithms is to ensure the tracking of the MPP of the PV system is reached regardless of the atmospheric conditions. Tracking the MPP using conventional methods has the advantage of simplicity in design and implementation. Still, these methods have a slow tracking response during rapid changes in temperature and/or irradiance levels. Intelligent algorithms can solve this problem because they can react quickly to sudden changes in atmospheric conditions [6,13,18]. However, the design and implementation of these algorithms involve a considerable degree of complexity. Thus, the motivation for this work is to propose a new controller with the advantages of simplicity in design like the conventional methods and intelligence techniques like intelligent algorithms. So, we can gather the benefits of both conventional and intelligent algorithms. The present work proposes a simple real-time controller called the SUIPID controller based on the multi-degree of freedom concept to get the MPP under uniform and varying atmospheric conditions, which can be used for a standalone charging station for electric vehicles. To test and assess the new algorithm's performance under varying atmospheric conditions, the SUIPID control was compared to three intelligent algorithms, such as the FLC-PSO, ANN, and FLC. The system simulation was first performed using MATLAB software, and then experimental work was set up to confirm the theoretical work. The novelty of this work can be summarized into the following aspects:

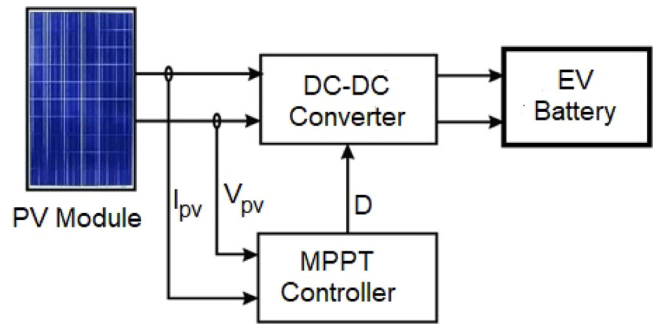


Fig. 1. PV system with battery charging.

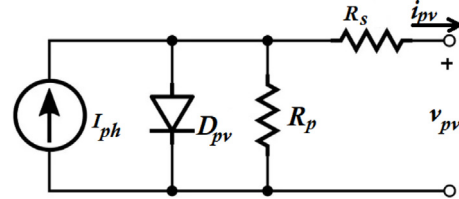


Fig. 2. Photovoltaic cell equivalent circuit.

1. Propose the new SUIPID controller based on the MDOF concept to extract the MPP from a PV system designed to meet the requirements of a battery charging system.
2. Test and evaluate the proposed controller compared with FLC-PSO, ANN, and FLC in terms of tracking the MPP according to the battery output voltage. Testing is performed both theoretically and experimentally in three cases:
 - A. Uniform irradiance and temperature levels.
 - B. Varying irradiance levels and consistent temperature levels.
 - C. Temperature fluctuations and consistent irradiance levels.

The structure of this article will be as follows; Section 2 introduces the modeling of the photovoltaic system with an EV battery. Section 3 presents the boost converter, while the FLC, FLC-PSO, ANN, and SUIPID will be proposed in Sections 4, 5, 6, and 7, respectively. Section 8 shows the EV battery modeling and simulation. Section 9 describes the simulation and experimental results, while the conclusions will be presented in Section 10.

2. Description of PV system

The photovoltaic battery charging system depicted in Fig. 1 was utilized in order to validate the MPPT algorithms that have been proposed. The photovoltaic module is composed of 60 series-connected cells that yield around 245 W, and the electrical parameters can be listed in Table 1. Different MPPT algorithms get the PV current and voltage measurements in order to adjust the converter's duty cycle (D), each using its own methodology, to attain the MPP. Additionally, the output from the converter can be directly linked to a direct current load, such as resistances or batteries, or connected to the utility grid. As indicated in Fig. 2, the photovoltaic cell can be used to describe a PV module. Using Kirchhoff's current law, the cell output current (i_{pv}) is given by [3–6]:

$$i_{pv} = I_{ph} - I_r \left[e^{q \frac{v_{pv} + i_{pv} R_s}{\eta K T}} - 1 \right] - \frac{v_{pv} + i_{pv} R_s}{R_p} \quad (1)$$

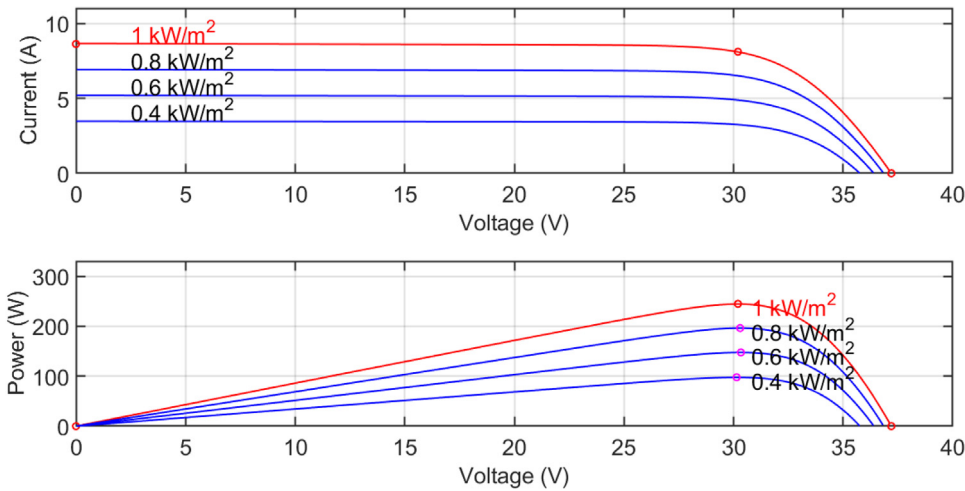


Fig. 3. PV characteristic under varying irradiance levels.

Table 1
Parameters of the 1Soltech 1STH-FRL-4H-245-M60-BLK module.

Electrical characteristics	Values
P_{max}	245 W
V_{max}	30.2 V
I_{max}	8.06 A
I_{SC}	8.81 A
V_{OC}	38.3 V

$$I_{ph} = [I_{SC} + \alpha(T - T_r)] \frac{G}{1000} \quad (2)$$

where I_{ph} : photocurrent of the cell in amperes (A), V_{pv} : output voltage from the cell in voltage (V), R_s : equivalent series resistance (Ω), R_p : equivalent parallel resistance (Ω), q : electron charge (1.6021×10^{-19} C), η : diode ideality factor of the p-n junction for the cell, K : Boltzmann constant (1.38×10^{-23} J/K), T : Cell surface temperature (°K), T_r : nominal temperature in Kelvin (reference temperature $T = 298.15$ °K), I_{SC} : short-circuit current in STC ($T_r = 298$ K and $G = 1000$ W/m²), α : temperature coefficient, G : solar irradiance (W/m²) and the reverse saturation current (I_r) can be calculated as

$$I_r = I_{r(STC)} \left(\frac{T}{T_r} \right)_e^3 \left[\frac{qEg}{\eta k} \left(\frac{1}{T_r} - \frac{1}{T} \right) \right] \quad (3)$$

$$I_{r(STC)} = \frac{I_{SC} - \frac{V_{OC}}{R_p}}{e^{\frac{qV_{OC}}{\eta kT_r}} - 1} \quad (4)$$

$$v_{pv} = v_{pv_Cell} N_s \quad (5)$$

$$V_{oc} = V_{oc_Cell} N_s \quad (6)$$

where $I_{r(STC)}$: reverse saturation current in STC (A), Eg : band gap energy in electron voltage (1.12 eV), v_{pv} : PV module voltage (V), N_s : No. of PV cells, V_{oc} : open-circuit voltage (V).

The module characteristics (power–voltage curve and current–voltage curve) under constant temperature (25 °C) and varying irradiation levels can be illustrated in Fig. 3.

3. Boost converter design

The converter transforms fluctuating direct current from a PV module to a steady fixed direct current. Fig. 4 illustrates the circuit diagram, which consists of the inductor, shunt IGBT switch, capacitor, and diode. The converter is powered by a field-effect

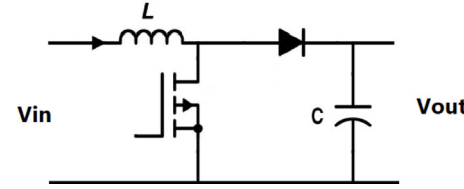


Fig. 4. Circuit diagram of the boost converter.

Table 2
Parameters of the converter.

Electrical Parameters	Values
Inductance	3.3 mH
Frequency	10 kHz
Capacitance	100 μF

transistor made of metal oxide semiconductors (MOSFET). The converter works in a cycle of period $1/f_s$, where f_s is the switching frequency. The cycle is composed of two modes; during the first mode, the MOSFET is switched ‘on’ and the diode reaches a reverse biased state during a time t , which is part of the cycle: $0 < t < D(1/f_s)$, where the duty D is less than 1. During that time the inductor L is charged by the voltage $V_L = V_{in}$. During the second mode, the MOSFET enters the ‘off’ state, which occupies the remaining part of the cycle $D(1/f_s) < t < (1/f_s)$. During that time the diode enters the ‘on’ state (forward bias) and the final output voltage $V_{out} = V_{dc} = V_{in} + V_L$. The design of the boost converter parameters can be calculated as [7–10]:

$$V_{out} = V_{dc} = \frac{V_{in}}{(1 - D)} \quad (7)$$

$$I_{out} = (1 - D)I_{in} \quad (8)$$

$$L = \frac{V_{in} * D}{f_s * \Delta I} \quad (9)$$

$$C = \frac{I_{out} * D}{f_s * \Delta V} \quad (10)$$

where I_{out} : output current of boost converter (A), ΔV : ripple in output voltage (V), ΔI : ripple in inductor current, V_{in} and I_{in} : input voltage (V) and current (A) respectively. The parameters of the converter are listed in Table 2.

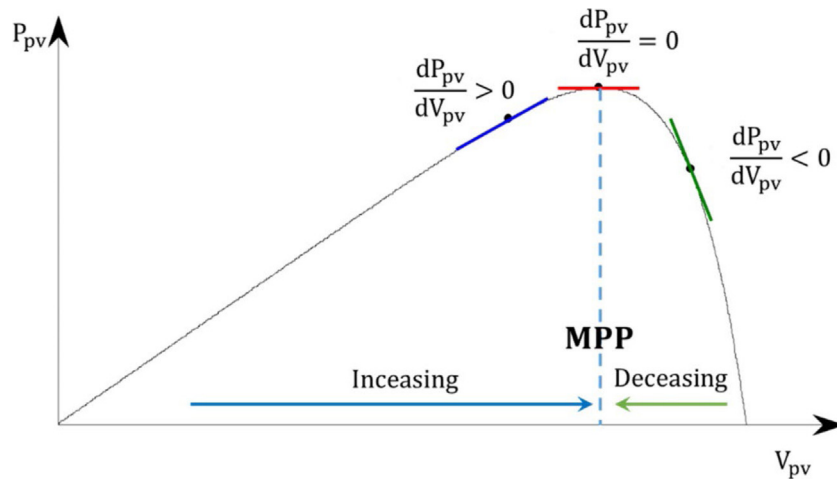


Fig. 5. P-V characteristic of a PV module.

4. MPPT via fuzzy logic controller

The fuzzy controller aims to obtain a good performance in tracking the MPP of the photovoltaic system by managing the duty cycle of the converter. The FLC detects the voltage and current at the output of the solar panel, which are the controller's inputs, and its output indicates the duty cycle. As seen in Fig. 5, the FLC adjusts the duty cycle of the converter based on the change in power relative to voltage (dP/dV) in order to increase or decrease the voltage until the power is maximum [15–17].

The fuzzy system has two inputs, the error signal and the change in error signal, and one output for the change in duty cycle to control the DC converter. The controller inputs and output are defined as follows:

$$E(k) = \frac{P(k) - P(k-1)}{V(k) - V(k-1)} \quad (11)$$

$$CE(k) = E(k) - E(k-1) \quad (12)$$

$$CD = f(E, CE) \quad (13)$$

where $P(k)$: instant power of the PV (W) and $V(k)$: instant voltage of the PV (V), CD : Change of the duty cycle, E : error signal (W/V), CE : Change in error signal.

The input error $E(k)$ shows whether the load operation point is to the right or left of the PV characteristic's MPP at an instant (K), whereas the change in error indicates the direction in which this point is moving. The design of the controller includes three essential parts: fuzzification, base rule, and defuzzification. Fig. 6 shows the input and output membership functions of the controller. Each membership function holds a more specific range and responds sensitively to the precise environment. For example, the range of the error signal was calculated by measuring the error signal (dP/dV) in different cases (different irradiance levels and/or temperatures) to get the most suitable range based on the fuzzy rule base. The range was set from -8.4 W/V to 8.4 W/V as the fuzzy was more sensitive at this range. Table 3 describes the rule base table of the fuzzy system, and Fig. 7 depicts the Simulink model of the system.

5. Optimization of the FLC

The PSO technique was proposed to optimize the membership functions (MFs) of the FLC to improve its performance. The input and output of the system are fixed at five MFs on a normalized universal model of discourse $[-1, 1]$, as shown in Fig. 8. Also,

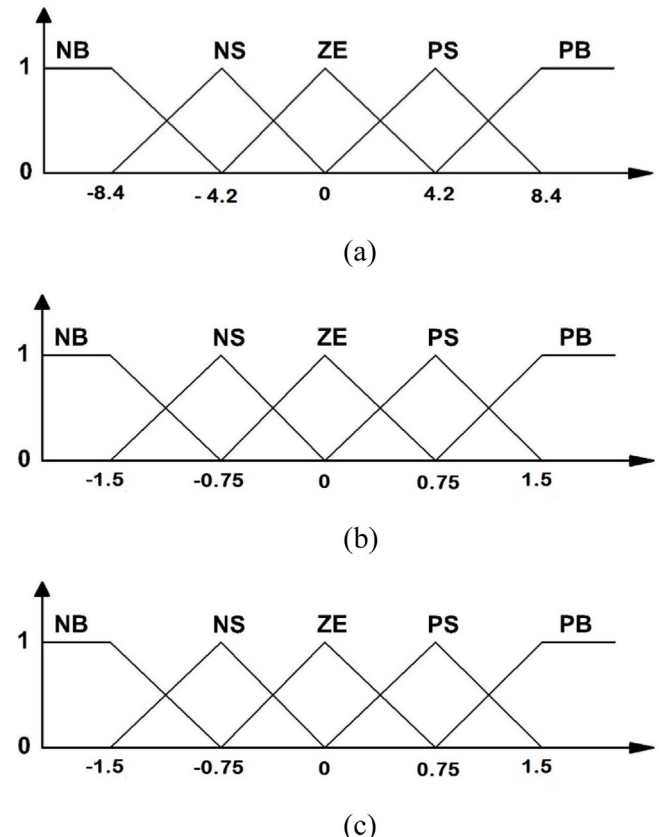


Fig. 6. Fuzzy system membership functions. (a) E. (b) CE. (c) CD.

Table 3

The rule base table of the fuzzy system.

E	CE					
		NB	NS	ZE	PS	PB
NB	PS	PB	NB	NB	NS	
NS	PS	PS	NS	NS	NS	
ZE	ZE	ZE	ZE	ZE	ZE	
PS	NS	NS	PS	PS	PS	
PB	NS	NB	PB	PB	PB	

the extremities are fixed on -1 and 1 , respectively, and the middle is centered on zero. Therefore, the means for all the

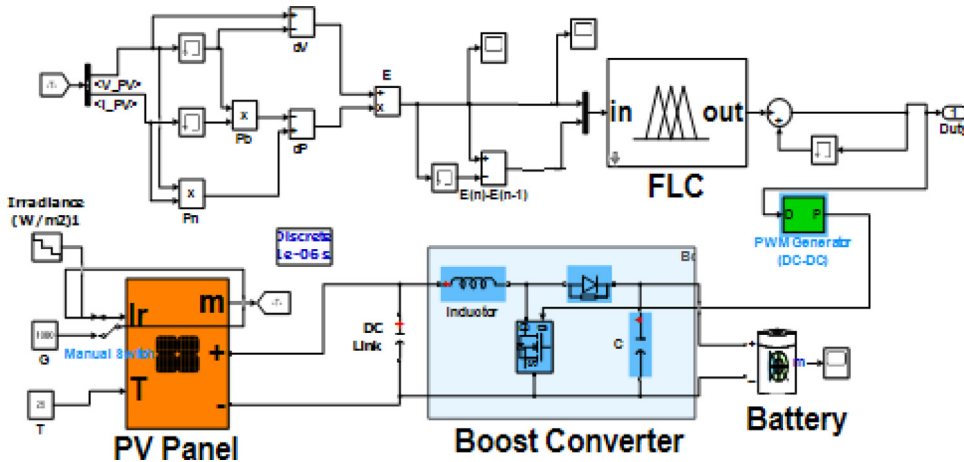


Fig. 7. Simulink model of the PV system with a fuzzy controller.

remaining functions and their variants need to be determined. Establishing a spacing parameter (*SPP*) for computing the means of the membership functions, as well as a middle deviation (σm) and an extreme deviation (σe) for calculating their deviations, are considered as follows [17,18].

A. Mean Parameter

The spacing parameter determines how the means of intermediate membership functions are separated from the center. If the *SPP* is greater than 1, the means are closer to the center; otherwise, the majority of means are distant from the center. At *SPP* = 1, the means in the universe of speech are evenly distributed $[-1, 1]$. The fuzzy rules were described previously in Table 3. Firstly, the means of uniformly distributed MFs, indicated by *CEQ(i)*, are calculated using the formula:

$$CEQ(i) = 2 \left(\frac{i-1}{NMFs-1} \right) - 1, \quad i = 1, \dots, NMFs \quad (14)$$

where: *NMFs* represents the total number of MFs and *i* represents the NB membership function and the means *C(i)* are calculated as:

$$C(i) = sign(CEQ(i)) * |CEQ(i)|^{SPP} \quad (15)$$

B. Deviation Parameter

To minimize the number of parameters while encoding all the deviations, a method employing a middle deviation (σm) and another denoted by (σe) for the middle MF (ZO) and those of the extremities (NB and PB), respectively. The deviations of intermediate MFs denoted by $\sigma(i)$ are computed from σm and σe with intermediate values at equal intervals and can be calculated as:

$$\sigma(i) = \sigma m + 2(i-1) \frac{(\sigma e - \sigma m)}{NMFs-1}, \quad i = 1, \dots, \frac{NMFs+1}{2} \quad (16)$$

$$\sigma(1) = \sigma m \text{ and } \sigma \left(\frac{NMFs+1}{2} \right) = \sigma e \quad (17)$$

Consequently, all MFs have been encoded using only three parameters, and with these three parameters, a huge variety of MF forms can be obtained.

Assume $P = [E_{SPP}, E_{\sigma m}, E_{\sigma e}, CE_{SPP}, CE_{\sigma m}, CE_{\sigma e}, CD_{SPP}, CD_{\sigma m}, CD_{\sigma e}]$ the PSO vector of optimization parameters and the target parameter *SPP* range for E, CE, and CD is [0.05, 2], while the target parameter range of σm and σe for E, CE, and CD is [0.05, 0.5].

An objective function directs the optimization algorithm's convergence toward the optimal global solution. Therefore, this last

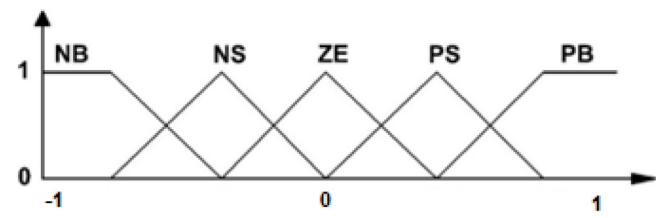


Fig. 8. Normalized membership function of the fuzzy for E, CE, and CD.

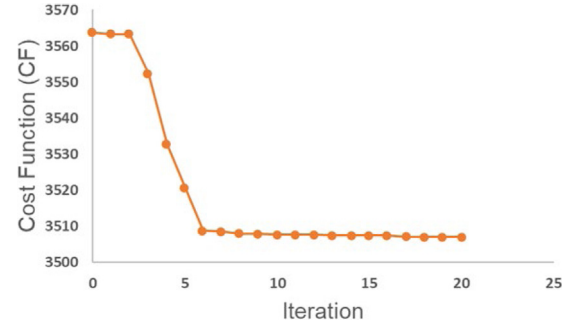


Fig. 9. The development of the cost function (CF).

must be accurately defined prior to algorithm execution. In this investigation, the objective function is specified as follows:

$$CF(n) = \sum_{j=1}^N |P_{pv_max}(j) - P_{pv}(j)| \quad (18)$$

where: *CF(n)*: Objective (cost or fitness) function, P_{pv_max} : maximum power (W) (considered as reference at $T = 25$, $G = 1000 \text{ W/m}^2$), P_{pv} : actual power of the *j*th sample (W), and *N*: number of samples. Table 4 shows the optimal parameter of the FLC. Fig. 9 depicts the evolution of the cost function during the PSO optimization process; after 20 iterations, PSO converges to the ideal values shown in Table 4. Fig. 10 shows the obtained membership functions for the E, CE, and CD corresponding to the optimal parameters.

6. MPPT via artificial neural network

Artificial intelligence techniques have several advantages over conventional techniques. The downsides of conventional methods

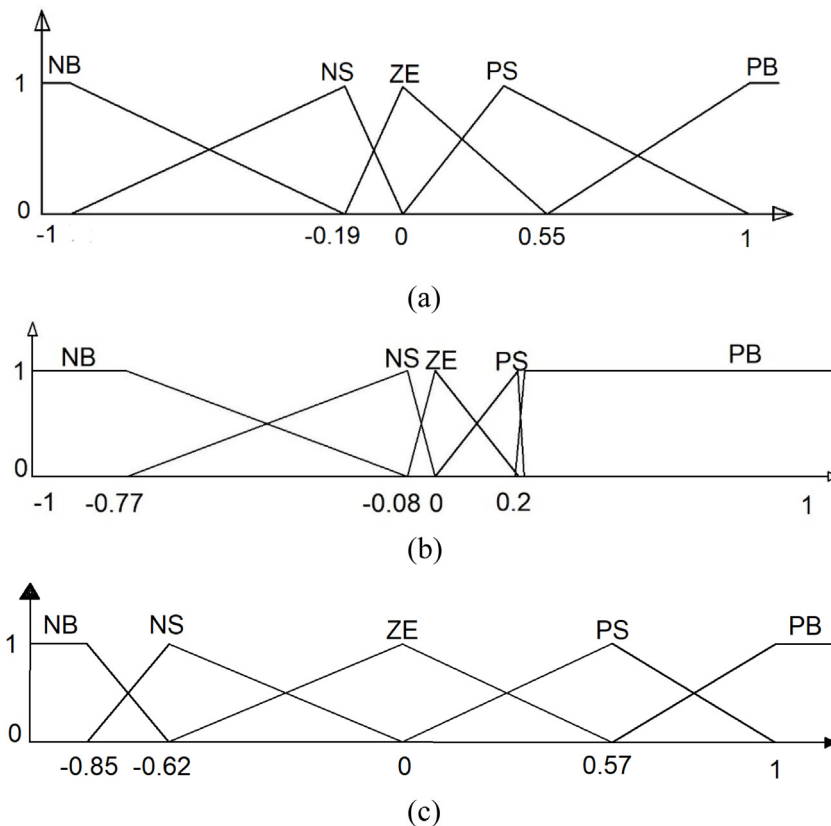


Fig. 10. Membership functions correspond to the optimal parameters. (a) E. (b) CE. (c) CD.

Table 4
FLC optimal sizing parameters.

Parameters	FLC – PSO
E_SSP	1.1058
E_σe	0.5000
E_σm	0.0501
CE_SSP	0.0627
CE_σe	0.05
CE_σm	0.4452
CD_SSP	0.0956
CD_σe	0.05
CD_σm	0.051

include their delayed response time to changes in solar temperature and irradiance conditions, and their occasional failure to track the highest power point. Fig. 11 shows a three-layer neural network used to get to the MPP. The input layer receives input data (irradiation and temperature); several hidden neurons receive data from the input layer and transmit it to the third layer via the second and hidden layers. The third layer provides output to the converter (duty cycle). The input and output can be expressed as [17,18]:

$$Y_j^h = f \left(\sum_{i=1}^N W_{ij} X_i + \theta_j^h \right) \quad (19)$$

$$Y_k^o = f \left(\sum_{j=1}^N W_{kj} Y_j^h + \theta_k^o \right) \quad (20)$$

where:

W_{ij} and W_{kj} : weights assigned to the lines connecting the three layers.

θ_j^h and θ_k^o : The bias values for the hidden layer and output layer respectively.

X_i and Y_j^h : Signal values for input and output lines.

Three processes are involved in creating an ANN: data collection, network structure determination, and training.

Data Collection: is used to train the ANN and is chosen to include a wide variety of temperatures and irradiance. For the PV module, ten levels of irradiation (100 W/m^2 to 1000 W/m^2) and four temperatures (0 C , 25 C , 45 C , and 65 C) are evaluated. By modeling the PV module under these conditions, it is possible to get the necessary training dataset.

Network structure determination: the structure of an ANN determines that its inputs and outputs are two and one, respectively. Trial and error are used to determine the number of neurons in each layer and the number of hidden layers (HL). In order to avoid complexity and overfitting the data, they should only be large enough to satisfy the threshold for fitting error.

Training: the network is trained using the Levenberg–Marquardt method, and its objective is to maximize the duty ratio of the converter. For each change in solar temperature and irradiance, the output from the neural network will have a unique duty ratio value to obtain the MPP. The best duty cycle is determined for various combinations of solar irradiation and temperature. Training of a neural network entails modifying the layer weights to obtain the desired results. During the training phase, weights are changed to ensure that they track the MPP values with the least amount of error possible.

The mean squared error (MSE) is the performance metric for ANNs. It is the average squared error between the outputs, a , and the target outputs, t . It calculated as

$$MSE = \frac{1}{N} \sum_{i=1}^N (e_i)^2 = \frac{1}{N} \sum_{i=1}^N (t_i - a_i)^2 \quad (21)$$

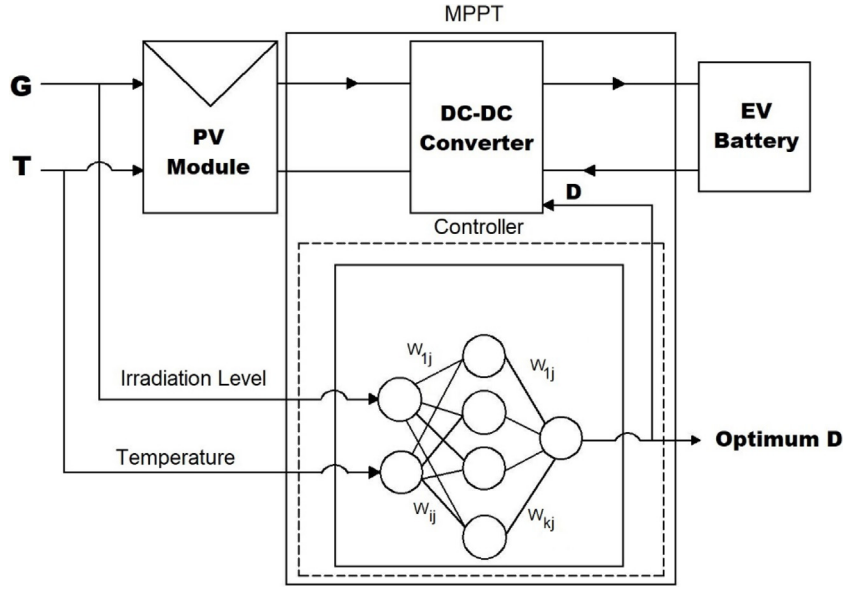


Fig. 11. Schematic diagram of MPPT system-based ANN.

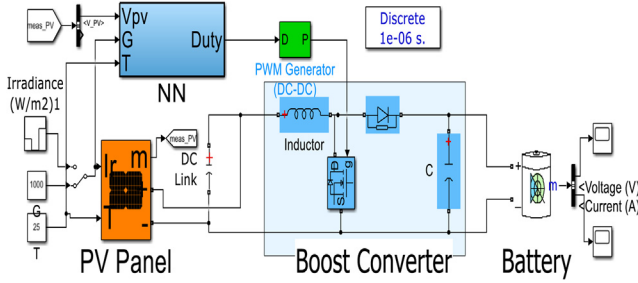


Fig. 12. Simulink model of the system with the ANN.

The final value of the MSE is 0.289, and the correlation coefficient is 0.996, indicating that the network has been properly trained.

The primary advantage of the ANN-based MPPT technique is that it may give adequate tracking accuracy for the MPP without requiring precise model parameter information. Its downside is that it must be prepared precisely for the photovoltaic system on which it will be installed. Additionally, because the PV system's P-V and I-V properties vary over time, the neural network must be trained at regular intervals to provide precise and efficient MPP tracking. Fig. 12 depicts Simulink model of the system.

7. Proposed MPPT via SUPIPID controller

The SUPIPID controller is the one proposed for the PV system with EV charging to get the MPP under varying operating conditions to overcome the drawbacks of both conventional and intelligent algorithms. Most contemporary intelligent algorithms are complex and require regular parameter updates throughout the operation. Additionally, they demand specialist personnel to deal with them rather than inexperienced consumers. As a result, most contemporary studies are attempting to simplify and improve the controller. Combining simplicity with intelligence is challenging because increasing the controller's intelligence inevitably results in an increase in system complexity. It is only possible to make the system smart or simple. However, both preceding objectives were accomplished using a newly suggested technology known as the SUPIPID controller [25]. The proposed

controller has the advantages that it uses a simple design algorithm and does not need to estimate the system's transfer function. Also, a modeling method does not have to calculate the PID controller constants like a regular PID controller. It is called an intelligent controller due to the self-adaptation of the controller constants during operation. So, this controller was chosen because it could combine the benefits of both traditional methods and intelligent algorithms due to its simple design and self-adaptation techniques. The controller design uses two steps: a simple PID controller and applying the concept of the MDOF using Eqs. (22) and (23), respectively. The MDOF is to utilize two controllers with two different gains working at the same time for both the wide range and fine-tuning regions of the error. The first controller output gain is tuned to realize the required rise time, and the second controller output gain is tuned for the steady-state error. Fig. 13 depicts the Simulink model of the system. For each of the two PIDs, having an input error signal e , PID controller constants (K_p , K_i , and K_d) are:

$$K_p : |e|; K_i : \left| \int e dt \right|; K_d : \left| \frac{d}{dt} e \right| \quad (22)$$

Finally, outputs of the two PIDs (O/P_1 , O/P_2) are combined to get final O/P as follows:

$$O/P = O/P_1 * Error + O/P_2(1 - Error) \quad (23)$$

The proposed input to the controller is a variation of the power relative to the voltage of the PV module, which describes the error signal term. The error signal can be handled under two controllers, and the final output from the two controllers is the duty cycle. The error signal is calculated the same way as in (11), reproduced here for further reference:

$$E(k) = \frac{P(k) - P(k-1)}{V(k) - V(k-1)} \quad (24)$$

The controller needs a normalization process for the error signal in order to maintain the error signal varying from zero to one as the maximum value. The error normalized can be described as

$$E_n = \frac{E(k) - E_{\min}}{E_{\max} - E_{\min}} \quad (25)$$

where E_n : normalized error signal (W/V); E_{\max} and E_{\min} : maximum and minimum value of the error signal (W/V) respectively.

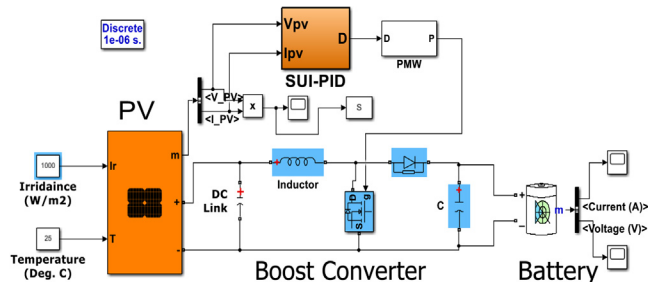


Fig. 13. Simulink model of the PV system with the SUIPID controller.

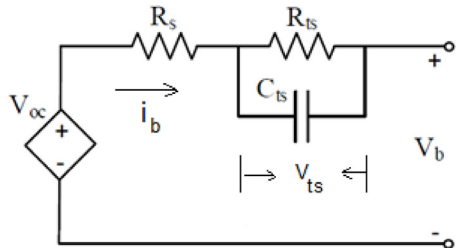


Fig. 14. Modeling of EV battery.

8. modeling of electric vehicle battery

The representation of an electric vehicle is through a battery that is recharged directly through the DC-DC converter. For the battery to operate smoothly, it must be modeled appropriately. Several battery models were used, including electrical, electrochemical, and mathematical models. For this investigation, the battery's electrical model is regarded as correct in terms of its features. The electrochemical behavior of a battery has been described in detail in [6], considering the internal resistance, state of charge (SOC), discharge current, and battery terminal voltage, among other factors. In general, an EV battery is a lithium-ion battery that meets the model's specs. The electric circuit is illustrated in Fig. 14. The specifications of the EV battery are reported in Table 5, and the EV battery is mathematically represented as [25,26]

$$V_b = V_{oc} - i_b R_s - V_{ts}; i_b = (V_{ts}/R_{ts}) + C_{ts} dV_{ts}/dt \quad (26)$$

where V_{oc} : EV constant voltage (V), V_b : EV battery voltage (V), i_b : EV battery current (A), R_s : battery resistance (Ω), and V_{ts} : The voltage of the RC network (V).

8.1. Battery capacity design

The capacity of the battery is referred to as the power consumption of a golf cart (Tesla Model 3) [27]. The energy required to run the cart for 1 km is about 0.15 kWh. The average power required for 30 km per day is about $0.15 \text{ kWh/km} * 30 \text{ km} = 4.5 \text{ kWh}$. To make the battery serve for one day, the energy necessary is 4500 Wh (battery capacity designed for 4800 Wh). To fully charge a completely exhausted golf cart battery in 10 h (the minimum sunlight hours of the year in Egypt), $0.15 \text{ kWh}/10 \text{ h} = 0.015 \text{ kW}$ must be generated by the solar panels per hour. In addition, to account for the 10% to 20% losses in the connections and DC/DC converter, the output power of the panels must be raised to achieve an hourly average of 0.018 kW. In other words, the average power output of the panels must be 0.018 kW. The average module power produced in 10 h = $245 \text{ W} * 10 \text{ h} = 2450 \text{ Wh}$, which matches the required daily power.

Table 5
EV battery parameters.

Type	Lithium-iron
Rating	80 Ah, 60 V
Max. discharge current	4.47 A
Max. charge current	4.0 A

Table 6
HIL probe configuration.

Electrical parameters	Probe
Power	100 W/div
Voltage	10 V/div
Current	1 A/div

Table 7
Comparison of the performance of several controllers.

	SUIPID	PSO-FLC	ANN	FLC
ITEA	0.08	0.11	0.17	0.23
Rising time	0.05 s	0.07	0.092 s	0.13 s
Settling time	0.07 s	0.09	0.11 s	0.16 s

The SOC is related to the energy stored in a system; it helps in describe the actual energy level available in the battery. The range of the SOC is from 20% to 95% and can be calculated as [1,7]

$$SOC(t+1) = SOC(t)\sigma + I_{bat}(t)\Delta t\eta (I_{bat}(t)) \quad (27)$$

where σ : self-discharging rate of battery rank, Δt : sampling period in seconds (s), $I_{bat}(t)$: batteries charging current (A), and $\eta (I_{bat}(t))$: charging current efficiency.

9. Theoretical and experimental results

Simulation and experimental work will be utilized to evaluate the proposed controller. In this study, simulations were carried out using MATLAB/Simulink, and an experimental set up was conducted to verify the simulated work. The experimental work involves the MicroLabBox platform (dSPACE1202), which performs the proposed SUIPID, PSO-FLC, ANN, and FLC. The hardware elements, such as the PV module, converter, and battery, each with their own parameters, were physically emulated using Typhoon HIL-402 [28]. The MicroLabBox platform and Typhoon HIL-402 should be connected through wiring connections. The MATLAB/Simulink program of the controllers and the parameters of each sub-system were uploaded using two supervisory control and data acquisition (SCADA) systems connected with the MicroLabBox and the HIL. The advantages of a SCADA system include controlling, monitoring, analyzing data, and getting the final output results. The probe configurations of the HIL for power, voltage, and current are listed in Table 6. Fig. 15 illustrates the experimental setup of the system, while Fig. 16 shows the block diagram for the system laboratory setup.

Fig. 17 shows the output PV power with the ANN, PSO-FLC, FLC and the proposed SUIPID under constant atmospheric conditions ($T = 25 \text{ }^{\circ}\text{C}$, $G = 1000 \text{ W/m}^2$). The SUIPID has a faster response, no overshoot, and a better rise time compared to ANN, FLC-PSO and FLC. With the SUIPID, the time taken to reach a steady state was 0.05 s, and the ANN controller was 0.11 s, while that with the FLC-PSO was 0.07 s and the FLC was 0.16 (i.e., 28.5%, 44.4%, and 61.5% better response compared to FLC-PSO, ANN, and FLC) under the battery charging conditions. Table 7 shows a comparative analysis of the performance of various controllers. The SUIPID has the best rising time, integral time absolute error (ITAE), and settling time compared to FLC-PSO, ANN, and FLC. In addition, the ITAE error was reduced by 27.3%, 52.9%, and 65.2%, respectively.

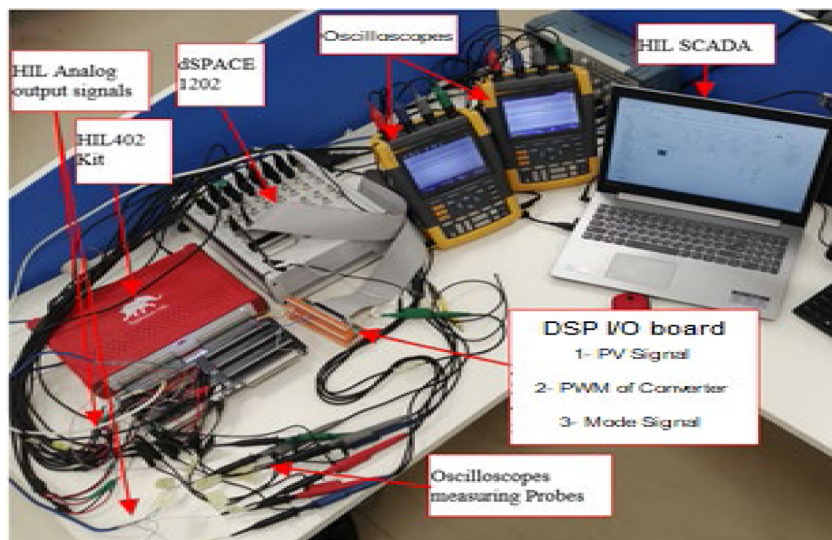


Fig. 15. Experimental setup of the system.

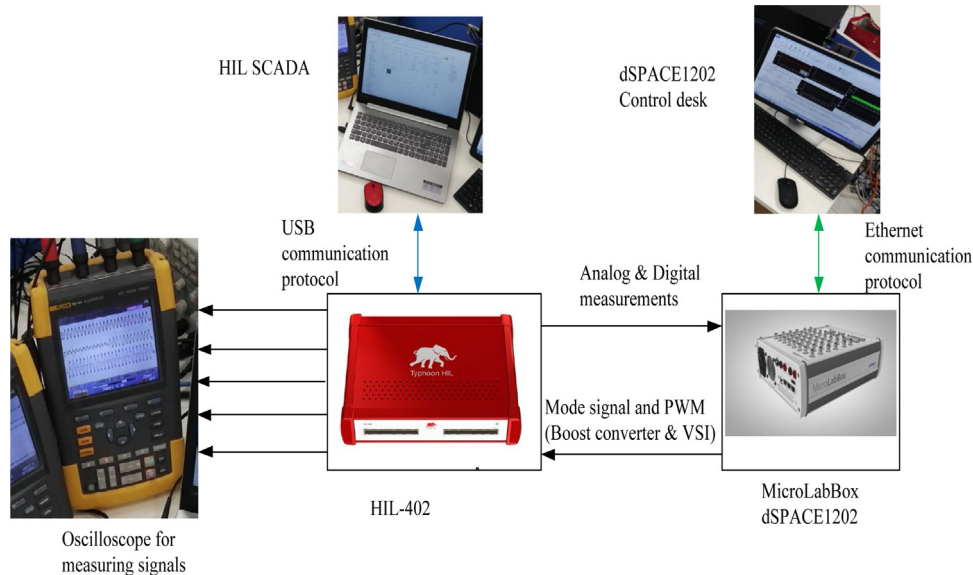


Fig. 16. Block diagram for the system laboratory setup.

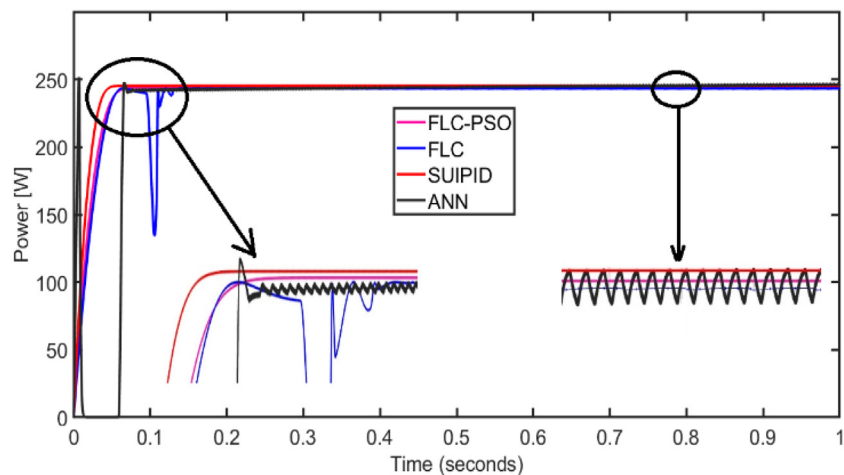


Fig. 17. Comparison study of the three controllers under constant atmospheric conditions ($T = 25 \text{ C}$, $G = 1000 \text{ W/m}^2$).

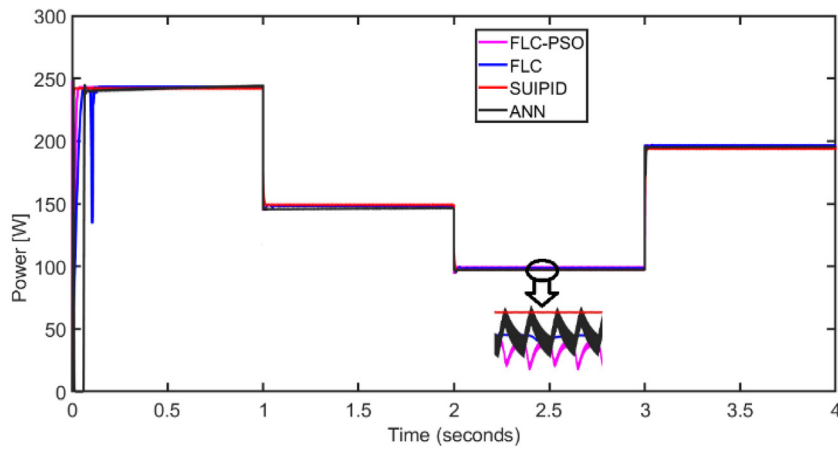


Fig. 18. Output power of the three controllers under constant temperature 25 C and different irradiance levels.

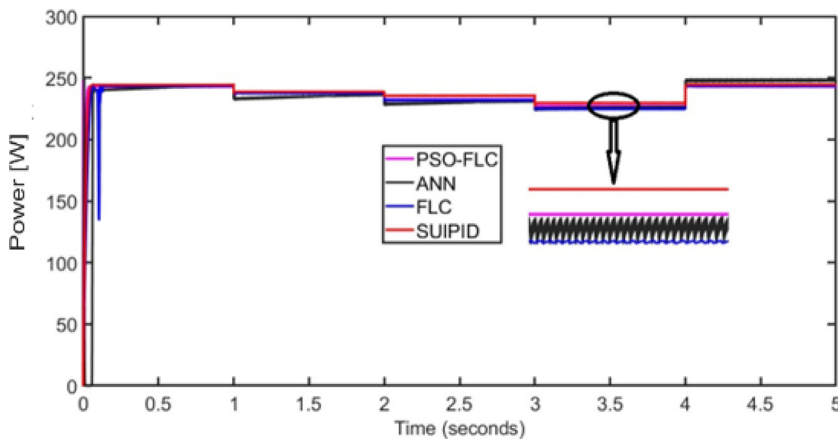


Fig. 19. Output power of the controllers under varying temperature and constant irradiance levels.

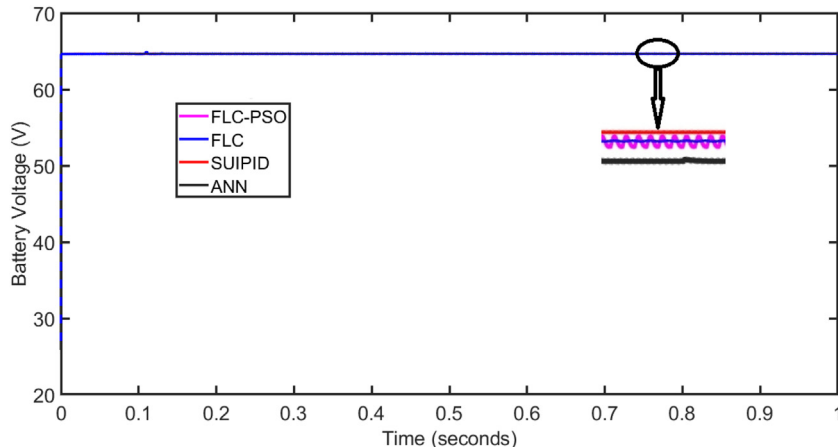


Fig. 20. A comparison study for the input voltage to the battery under varying irradiation levels for different controllers.

Fig. 18 illustrates the theoretical PV output power under a sudden decrease in the irradiance levels from 1000 W/m^2 to 600 W/m^2 , then to 400 W/m^2 , and finally back to 800 W/m^2 for the four controllers. It can be observed that their capacity to track the MPP under the four controllers is superior. However, the SUIPID has smaller rise and settling times in addition to the simplicity in design and implementation.

Fig. 19 illustrates the theoretical PV output power under varying temperature levels and constant in the irradiance levels of

1000 W/m^2 for the four controllers. The temperature varied from 25 C to 30 C then 35 C next 40 C and finally back to 25 C. It can be observed that their capacity to track the MPP under the four controllers is superior. However, the SUIPID has smaller rise and settling times in addition to the simplicity in design and implementation.

Fig. 20 illustrates the theoretical effects of the decreasing or increasing of the irradiance levels with SUIPID, FLC-PSO, ANN, and FLC on the input voltage to the battery. The voltage rating

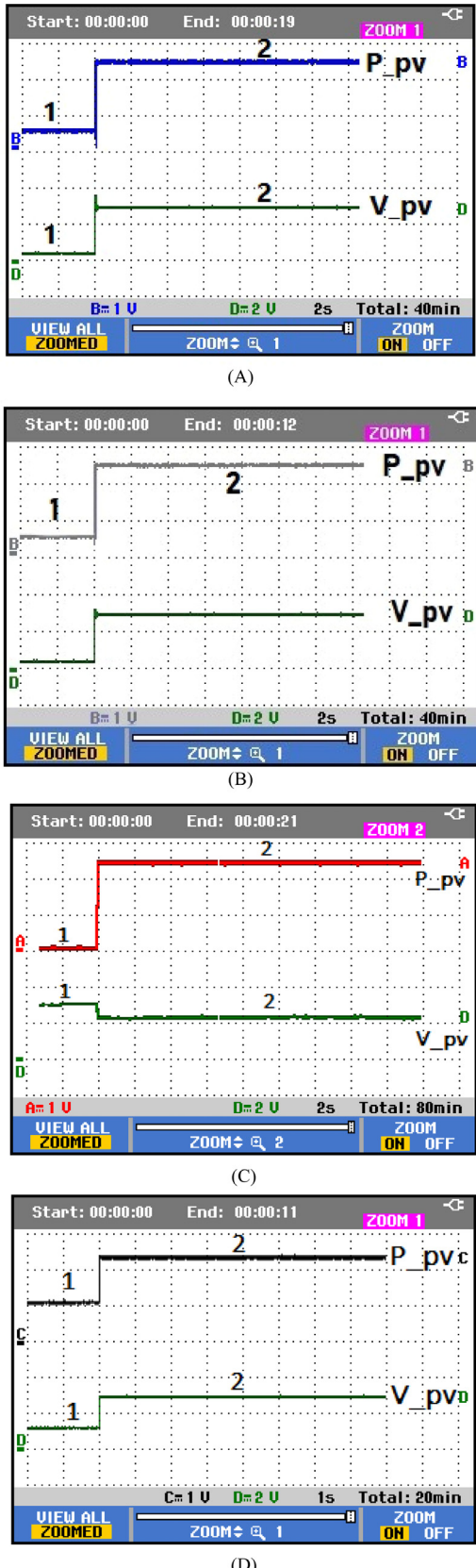


Fig. 21. Power and voltage of the PV module under uniform atmospheric conditions. (A) SUIPID. (B) PSO-FLC. (C) ANN. (D) FLC.

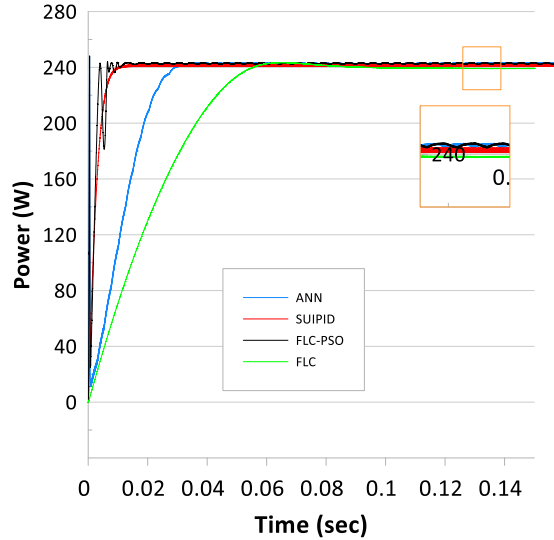


Fig. 22. Experimental comparison study of the output power for all controllers under constant atmospheric conditions ($T = 25\text{ C}$, $G = 1000\text{ W/m}^2$).

for the battery was set at 60 V, and in the charging case, the module should provide more than the rated voltage to the battery, for example, 65 V. The results show the steady charging process for all the controllers during the variation in irradiance levels. The voltage level remains constant during the variations in irradiance levels. However, the SUIPID is simpler in design and implementation.

Fig. 21A, B, C, and D display the experimental output power and voltage results from the PV system with the SUIPID, FLC-PSO, ANN, and FLC under constant atmospheric conditions ($T = 25\text{ C}$, $G = 1000\text{ W/m}^2$). The figures pass into two regions: no control action mode (area 1) and control action mode (area 2). In the absence of control signal, a fixed duty cycle is applied to the converter. All controllers show a steady power and voltage level under constant atmospheric conditions. However, the SUIPID controller is simpler in design and implementation.

Fig. 22 shows the experimental output power from the PV system with the SUIPID, FLC-PSO, ANN, and FLC under constant atmospheric conditions ($T = 25\text{ C}$, $G = 1000\text{ W/m}^2$). The experimental output power data for all controllers were extracted and plotted on a single graph. All intelligent controllers have an excellent ability to track the MPP. However, the SUIPID controller has the best response time, minimum overshoot, and a better rise time than FLC-PSO, ANN, and FLC. However, the SUIPID controller is simpler in design and implementation.

Fig. 23A, B, C, and D display the effects of decreasing or increasing the irradiance levels on the PV output power and voltage with SUIPID, FLC-PSO, ANN, and FLC, respectively. The irradiance levels vary from 1000 W/m^2 (area 2) to 500 W/m^2 (area 3), and finally back to 1000 W/m^2 (area 4), and the control action goes off in area 1. The results show superior performance for tracking the MPP with the four controllers under varying irradiation levels. However, the SUIPID has smaller oscillations in the voltage level, in addition to its simplicity in design and implementation.

Fig. 24A, B, C, and D display the effects of decreasing or increasing the temperature levels on the PV output power and voltage with SUIPID, FLC-PSO, ANN, and FLC, respectively. The levels vary from 25 C (area 1) to 35 C (area 2), then 45 C (area 3), and finally back to 25 C (area 4). The results show superior performance for tracking the MPP with the four controllers under varying temperature levels. The output power remains steadier

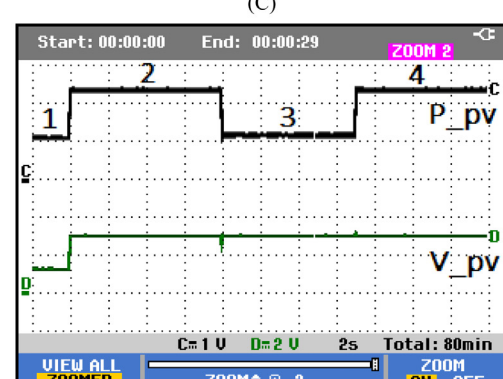
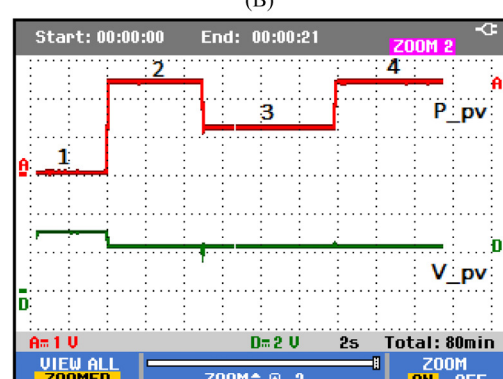
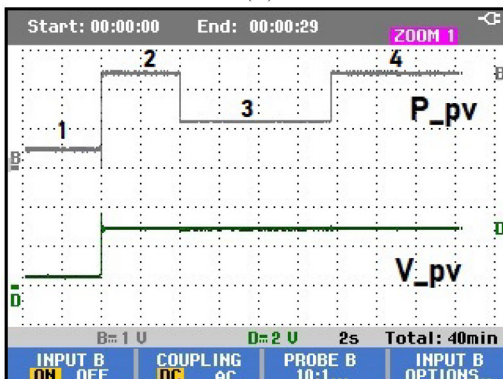
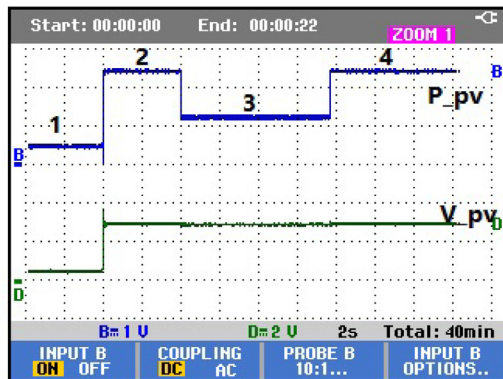


Fig. 23. Power and voltage of the PV module under varying irradiation levels and constant temperature. (A) SUPIP. (B) PSO-FLC. (C) ANN. (D) FLC.

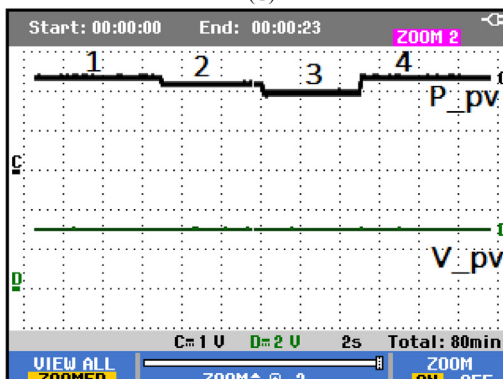
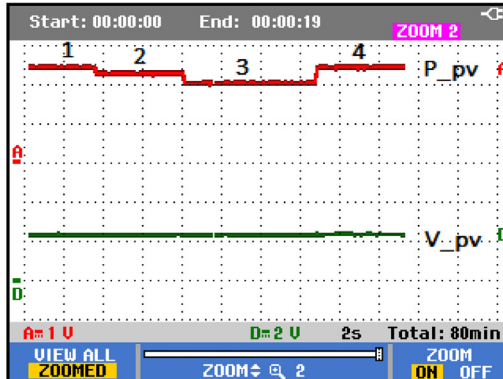
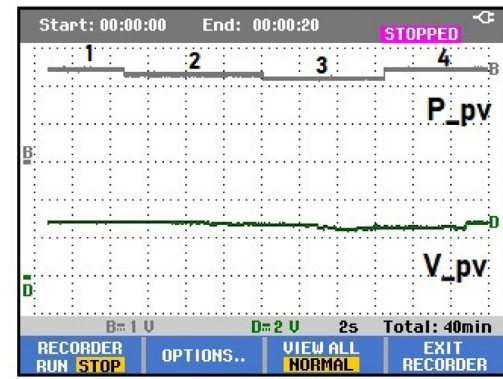
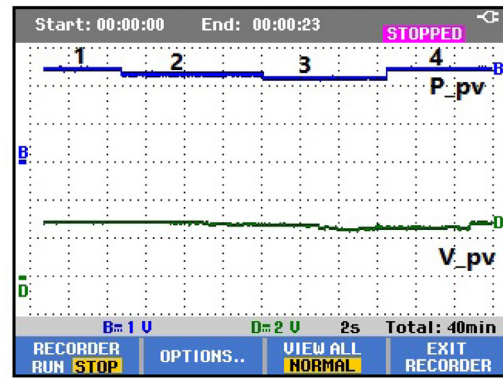


Fig. 24. Power and voltage of the PV module under varying temperature levels and constant irradiation. (A) SUPIP. (B) PSO-FLC. (C) ANN. (D) FLC.

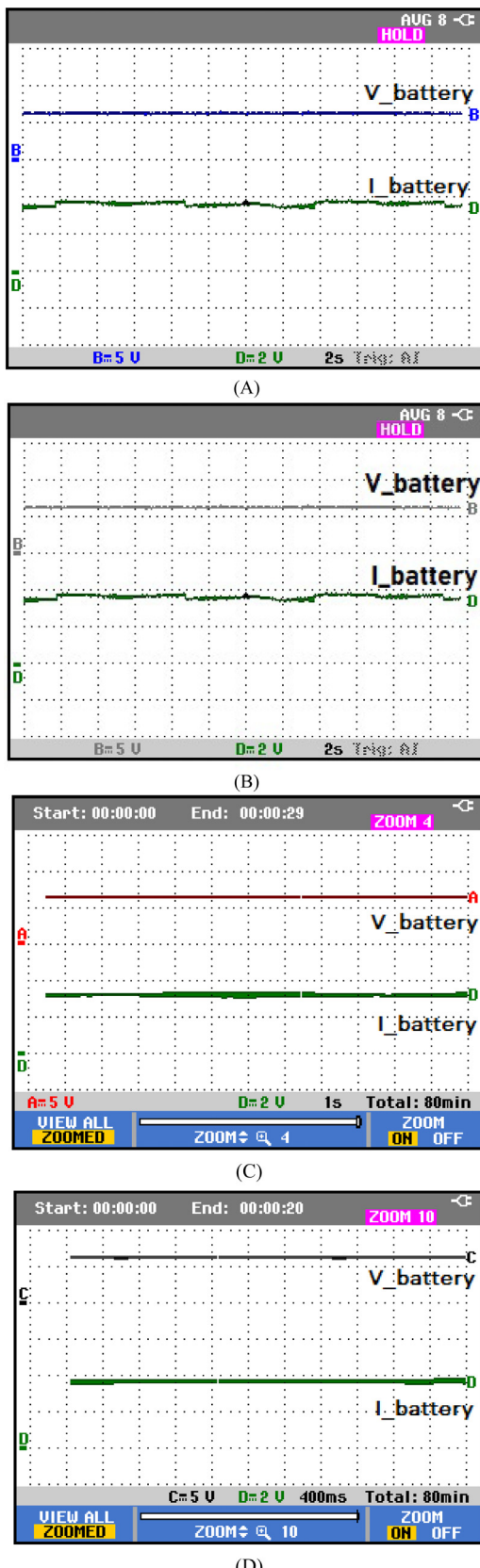


Fig. 25. Battery voltage and current under varying irradiation levels and constant temperature. (A) SUIPID. (B) PSO-FLC. (C) ANN. (D) FLC.

with the SUIPID controller compared to FLC-PSO, ANN and FLC. Furthermore, the simplicity in design and implementation.

Fig. 25A, B, C, and D display the effects of the increasing or decreasing of the irradiance levels with SUIPID, FLC-PSO, ANN, and FLC on the EV battery voltage and current. The results show the steady charging process for all the controllers during the variation in irradiance levels. The voltage remains constant during varying irradiance levels. However, the SUIPID is simpler in design and implementation.

10. Conclusions

A new controller was proposed to extract the MPP from the PV system to charge the EV's battery. The MPPT was extensively investigated using four controllers under varying operating conditions. These controllers are the FLC, PSO-FLC, ANN, and the proposed SUIPID controller. The configuration of the hardware has been emulated using Typhoon HIL-402, and the four controllers were performed using the MicroLabBox dSPACE1202 platform. According to the theoretical and experimental results, the following conclusions can be extracted:

- The EV battery charges steadily and without interruption under uniform and varying atmospheric conditions for all controllers. However, the SUIPID controller has the best response with fewer oscillations than PSO-FLC, ANN, and FLC.
- Faster response and better rise time were achieved by using the SUIPID controller compared to the PSO-FLC, ANN, and FLC. The SUIPID controller has no overshoot, a faster response, and a better rise time than ANN, FLC-PSO, and FLC. With the SUIPID, the time taken to reach a steady state was 0.05 s, and the ANN controller was 0.11 s, while that with the FLC-PSO was 0.07 s, and the FLC was 0.16 (i.e., 28.5%, 44.4%, and 61.5% better response compared to the FLC-PSO, ANN, and FLC, respectively).
- The SUIPID controller provides superior performance for tracking the MPP during abrupt changes in irradiance and temperature compared with ANN, PSO-FLC, and FLC.
- The SUIPID controller is considered the best choice to track the MPPT regarding its simplicity and intelligence compared to FLC-PSO, ANN, and FLC. The error measured by the ITAE was 27.3%, 52.9%, and 65.2% lower, respectively.

Declaration of competing interest

The authors declare that they have no known competing financial interests or personal relationships that could have appeared to influence the work reported in this paper.

References

- Kraiem H, Flah A, Mohamed N, Alowaidi M, Bajaj M, Mishra S, Sharma SK. Increasing electric vehicle autonomy using a photovoltaic system controlled by particle swarm optimization. *IEEE Access* 2021;9:72040–54.
- Arul PG, Ramachandaramurthy VK. Mitigating techniques for the operational challenges of a standalone hybrid system integrating renewable energy sources. *Sustain Energy Technol Assess* 2017;22:18–24.
- He F, Fathabadi H. Novel standalone plug-in hybrid electric vehicle charging station fed by solar energy in presence of a fuel cell system used as supporting power source. *Renew Energy* 2020;156:964–74.
- Nehrir MH, Wang C, Strunz K, Aki H, Ramakumar R, Bing J, Salameh Z. A review of hybrid renewable/alternative energy systems for electric power generation: Configurations, control, and applications. *IEEE Trans Sustain Energy* 2011;2(4):392–403.
- Mansour AM, Arafa OM, Marei MI, Abdelsalam I, Aziz GAA, Sattar AA. Hardware-in-the-loop testing of seamless interactions of multi-purpose grid-tied PV inverter based on SFT-PLL control strategy. *IEEE Access* 2021;9:123465–123483.

- [6] Pathak PK, Yadav AK. Design of battery charging circuit through intelligent MPPT using SPV system. *Sol Energy* 2019;178:79–89.
- [7] Ibrahim SA, Nasr A, Enany MA. Maximum power point tracking using ANFIS for a reconfigurable PV-based battery charger under non-uniform operating conditions. *IEEE Access* 2021;9:114457–114467.
- [8] Fathabadi H. Novel solar powered electric vehicle charging station with the capability of vehicle-to-grid. *Sol Energy* 2017;142:136–43.
- [9] El-Khatib MF, Shaaban S, El-Sebah MIA. A proposed advanced maximum power point tracking control for a photovoltaic-solar pump system. *Sol Energy* 2017;158:321–31.
- [10] Kavya M, Jayalalitha S. A novel coarse and fine control algorithm to improve Maximum Power Point Tracking (MPPT) efficiency in photovoltaic system. *ISA Trans* 2022;121:180–90.
- [11] Ahmed J, Salam Z. An improved perturb and observe (P & O) maximum power point tracking (MPPT) algorithm for higher efficiency. *Appl Energy* 2015;150:97–108.
- [12] Zakzouk NE, Elsaharty MA, Abdelsalam AK, Helal AA, Williams BW. Improved performance low-cost incremental conductance PV MPPT technique. *IET Renew Power Gener* 2016;10(4):561–74.
- [13] Bendib B, Belmili H, Krim F. A survey of the most used MPPT methods: Conventional and advanced algorithms applied for photovoltaic systems. *Renew Sustain Energy Rev* 2015;45:637–48.
- [14] Yatimi H, Aroudam E. MPPT algorithms based modeling and control for photovoltaic system under variable climatic conditions. *Procedia Manuf* 2018;22:757–64.
- [15] Dounis AI, Kofinas P, Alafodimos C, Tseles D. Adaptive fuzzy gain scheduling PID controller for maximum power point tracking of photovoltaic system. *Renew Energy* 2013;60:202–14.
- [16] Bendib B, Krim F, Belmili H, Almi MF, Boulouma S. Advanced fuzzy MPPT controller for a stand-alone PV system. *Energy Procedia* 2014;50:383–92.
- [17] Farajdadian S, Hosseini SH. Optimization of fuzzy-based MPPT controller via metaheuristic techniques for stand-alone PV systems. *Int J Hydrogen Energy* 2019;44(47):25457–72.
- [18] Kermadi M, Berkouk EM. Artificial intelligence-based maximum power point tracking controllers for photovoltaic systems: Comparative study. *Renew Sustain Energy Rev* 2017;69:369–86.
- [19] Jiang LL, Maskell DL, Patra JC. A novel ant colony optimization-based maximum power point tracking for photovoltaic systems under partially shaded conditions. *Energy Build* 2013;58:227–36.
- [20] Liu YH, Huang SC, Huang JW, Liang WC. A particle swarm optimization-based maximum power point tracking algorithm for PV systems operating under partially shaded conditions. *IEEE Trans Energy Convers* 2012;27(4):1027–35.
- [21] Kaced K, Larbes C, Ramzan N, Bounabi M, elabadine Dahmane Z. Bat algorithm based maximum power point tracking for photovoltaic system under partial shading conditions. *Sol Energy* 2017;158:490–503.
- [22] Daraban S, Petreus D, Morel C. A novel MPPT (maximum power point tracking) algorithm based on a modified genetic algorithm specialized on tracking the global maximum power point in photovoltaic systems affected by partial shading. *Energy* 2014;74:374–88.
- [23] Mohanty S, Subudhi B, Ray PK. A new MPPT design using grey wolf optimization technique for photovoltaic system under partial shading conditions. *IEEE Trans Sustain Energy* 2015;7(1):181–8.
- [24] Mohanty S, Subudhi B, Ray PK. A grey wolf-assisted perturb & observe MPPT algorithm for a PV system. *IEEE Trans Energy Convers* 2016;32(1):340–7.
- [25] Sebah MIAE. Simplified universal intelligent PID controller. *Int J Eng Res* 2016;5(1):11–5.
- [26] Fathabadi H. Novel battery/photovoltaic hybrid power source for plug-in hybrid electric vehicles. *Sol Energy* 2018;159:243–50.
- [27] <https://ecocostsavings.com/electric-car-kwh-per-mile-list/>.
- [28] <https://www.typhoon-hil.com/doc/products/Typhoon-HIL402-brochure.pdf>.